



Sunlight-driven photoelectrochemical sensor for direct determination of hexavalent chromium based on Au decorated rutile TiO₂ nanorods



Roozbeh Siavash Moakhar^{a,b}, Gregory Kia Liang Goh^{b,*}, Abolghasem Dolati^a, Mohammad Ghorbani^{a,*}

^a Department of Materials Science and Engineering, Sharif University of Technology, Tehran, 11155-9466, Iran

^b Institute of Materials Research and Engineering, Agency for Science, Technology and Research (A*STAR), 3 Research Link, 117602, Singapore

ARTICLE INFO

Article history:

Received 29 March 2016
Received in revised form 24 July 2016
Accepted 15 August 2016
Available online 16 August 2016

Keywords:

Photoelectrochemical sensor
Hexavalent chromium
TiO₂ rutile nanorods
Gold nanoparticles

ABSTRACT

A highly sensitive and selective sunlight-driven photoelectrochemical sensor for the direct detection and reduction of chromium(VI) was developed based on single crystal rutile titanium dioxide nanorods decorated with gold nanoparticles. Under sun simulator illumination via the amperometric technique, these Au decorated TiO₂ photoelectrodes exhibited the highest sensitivity ($13.94 \mu\text{A } \mu\text{M}^{-1}$) ever reported among Au-based electrodes for Cr(VI) detection, with a very low detection limit ($S/N=3$) of $0.006 \mu\text{M}$ and wide linear concentration range from $0.01 \mu\text{M}$ to $50 \mu\text{M}$. Measurements in real water samples such as laboratory and river water also showed excellent anti-interference and recovery capabilities.

© 2016 Elsevier B.V. All rights reserved.

1. Introduction

Heavy soil and water pollution caused by hexavalent chromium ions (Cr(VI)) leads to it being recognized as one of the most dangerous threats to humans and the environment [1]. Chromium is mainly found in the two stable states of Cr(III) and Cr(VI). The former is a harmless but vital micronutrient for fat and glucose metabolism and proper functioning of insulin [2]. On the other hand, Cr(VI) is well known as a carcinogen, genotoxic and mutagen agent even in trace amounts as it can enter cells via the sulphate transport system and oxidatively damage DNA and other cell components [3,4]. It is therefore critical to develop a novel protocol that can effectively detect trace levels of Cr(VI) in contaminated groundwater and reduce it to less toxic Cr(III).

Inductively coupled plasma mass spectrometry [5], chromatography [6], co-precipitation [7], electrochemical analysis [8,9] and spectrophotometry [10] are common methods for Cr(VI) detection. Nevertheless, these techniques suffer from at least one unfavorable limitation including being too time-consuming, requiring expensive laboratory equipment, non-portability, low sensitivity and/or low selectivity. By contrast, photocatalytic reduction of Cr(VI) based on TiO₂ nanostructures has been shown to be a promising

treatment technology due to the low cost, nontoxicity, good chemical stability, high photocatalytic activity, and reusability of TiO₂ [11,12]. There exist quite a few published reports on the reduction of Cr(VI) by conventional photocatalysis using TiO₂ nanostructures [13–16]. Nonetheless, the recombination of photogenerated carriers is still a great challenge to tackle as it leads to low quantum efficiency [17].

Recently, photoelectrochemical (PEC) analysis successfully reduced the recombination rate of photogenerated electrons and holes, and became an alternative to conventional analytical methods. The PEC sensing method possesses unique benefits such as rapid turnaround times, low cost, convenient instrumentation and ease of miniaturization [18,19]. Moreover, separation between the excitation source (light) and detection (photocurrent) offers high sensitivity with low undesired background noise. PEC sensing involves electron transfer between analyte, semiconductor, and electrode under photo-illumination [20] of which the interaction between the analyte and the illuminated semiconductor leads to a change in photocurrent. As a result, PEC sensors combine the advantages of both electrochemical and optical sensors by fully coupling photoirradiation with electrochemical signals [19].

Despite having the mentioned advantages, it is surprising that not a significant amount of study has been carried out in this field [18,21,22]. Specifically, to the best of our knowledge, there exists only one other study [23] that utilizes PEC sensors for Cr(VI) detection. In that research, Li et al. [23] introduced an indirect PEC Cr(VI) sensor based on its redox reaction with quercetin. Although this

* Corresponding authors.

E-mail addresses: g-goh@imre.a-star.edu.sg (G.K.L. Goh), ghorbani@sharif.edu (M. Ghorbani).

was a promising investigation, the linear concentration range was significantly limited (0.001–0.01 μM and 0.02–0.14 μM), preventing practical applications.

Here, a novel PEC approach is proposed for the direct sensing and reduction of Cr(VI) based on single crystal rutile TiO_2 nanorods decorated with Au nanoparticles. The proposed protocol exhibits a high sensitivity of $13.94 \mu\text{A} \mu\text{M}^{-1}$ and a very low detection limit ($S/N = 3$) of $0.006 \mu\text{M}$. The PEC sensor for Cr(VI) detection opens new perspectives for the application of TiO_2 nanorod-based PEC sensors for direct detection of other heavy metal contaminants.

2. Experimental

2.1. Materials

Titanium butoxide (99.0%), gold (III) chloride trihydrate ($\geq 49.0\%$ Au basis), hydrochloric acid (37%), acetone and ethanol were purchased from Sigma Aldrich and used without further treatment. Fluorine doped tin oxide (FTO) coated glass substrates (TEC 15 Pilkington TEC GlassTM, $10 \Omega/\text{square}$) were supplied by Nippon Sheet Glass, Japan and was ultrasonically cleaned for 30 min in a mixed solution of detergent, deionized water, acetone, and 2-propanol, with volume ratios of 1:1:1:1, respectively. All aqueous solutions were prepared with Millipore water (Milli-Q).

2.2. Apparatus

All electrochemical experiments were performed in a conventional three-electrode cell using Autolab 302N potentiostat/galvanostat equipped with FRA32M. Pristine and Au nanoparticle decorated TiO_2 nanorod photoelectrodes were used as the working electrode, while a saturated calomel electrode (SCE) and platinum-sheet served as the reference and counter electrodes, respectively. Electrochemical Impedance Spectroscopy (EIS) was carried out at open circuit potentials, in a frequency range of 1 mHz–10 kHz, with potential amplitude of 10 mV in a 0.1 M KCl solution containing 5 mM $\text{K}_3[\text{Fe}(\text{CN})_6]$. The $R(\text{C}(\text{RW}))$ equivalent circuit was used to fit the data with the Nova 1.10 software. The surface morphology was studied with field emission scanning electron microscope (FESEM JEOL JSM7600F). High resolution transmission electron microscopy (HRTEM) images were obtained with a JEOL 2100 HRTEM at an accelerating voltage of 200 kV. X'Pert Pro MPD (PANalytical) was used to study the crystal structure of samples with $\text{Cu K}\alpha$ radiation ($\lambda = 1.54 \text{\AA}$). X-ray photoelectron spectroscopy (XPS) experiments were carried out using ESCA Lab 250i-XL with $\text{Al K}\alpha$ X-ray source ($E = 1486.6 \text{ eV}$). Finally, UV-vis absorption spectra were recorded using a UV-3101PC UV-vis spectrophotometer.

2.3. Photoelectrode preparation

Synthesis of TiO_2 nanorods was carried out using a facile hydrothermal method as described elsewhere [24]. Briefly, 12 mL of hydrochloric acid and 12 mL of deionized water were mixed and stirred at ambient conditions for 10 min, then 1 mL of titanium butoxide was added dropwise. The solution was gently transferred to the Teflon-lined stainless steel autoclave (100 mL total volume, Parr Instrument Co.), where a FTO glass substrate ($3 \times 1 \text{ cm}^2$) was placed at 45° against the wall with the conducting side facing down. The hydrothermal synthesis was conducted at 150°C for 14 h in an oven. After synthesis, the autoclave was cooled to room temperature in air for 30 min. The FTO glass substrate was removed, rinsed with deionized water and dried with N_2 .

Decoration of the TiO_2 nanorods with Au nanoparticles was done using the cyclic voltammetry (CV) technique at a scan rate

of 20 mV s^{-1} for 1, 2, 4 and 8 cycles in a de-aerated solution containing 1 mM HAuCl_4 . After deposition, a change in the color of the photoelectrodes from white to light violet was observed. The samples were labeled as $\text{Au-TiO}_2\text{-}n$, where n represented the number of Au electrodeposition cycles.

2.4. Photoelectrochemical reduction of Cr(VI)

Measurement of the photoresponse was done using the chronoamperometry technique under chopped simulated solar light irradiation (100 mW cm^{-2} , light on/off cycles: 30 s) at a bias potential of -0.2 V vs. SCE in an aqueous solution containing 0.1 mM HCl as a supportive electrolyte, with different concentrations of $\text{K}_2\text{Cr}_2\text{O}_7$. All the electrolytes were deaerated with Ar for 60 min prior to each measurement and kept under Ar atmosphere during the period of the test. For UV only and visible only light illumination, two optical filters, $330 \pm 70 \text{ nm}$ for UV and $520 \pm 46 \text{ nm}$ for visible were used. Photocurrents used in analysis are presented as i_{net} , which is the increase in steady state photocurrent measured before and after Cr(VI) additions.

For comparison, photocatalytic reduction of Cr(VI) method was also conducted under simulated solar light irradiation. Prior to illumination, 200 mL of 50 mg/L $\text{K}_2\text{Cr}_2\text{O}_7$ aqueous solution containing 0.2 g of photocatalyst was magnetically stirred in the dark for 2 h. During illumination, about 3 mL of suspension was taken from the reactor at a specific interval and centrifuged to separate the photocatalyst. For both PEC and photocatalytic processes, the concentration of Cr(VI) was measured by UV-vis spectrophotometer, where Cr(VI) was determined at 540 nm according to the diphenylcarbazide colorimetric method using the following expression:

$$\text{Reduction ratio of Cr(VI)} = (C_0 - C_t)/C_0 \times 100 \quad (1)$$

where C_0 and C_t are the absorbance intensities when illuminated for 0 (that is, just after the dark adsorption) and t min, respectively. Each experiment was performed 3 times to certify reproducibility.

For measurement of natural media, tap water was gathered directly from the laboratory without any further treatment, while river water was collected from the Karaj River in Iran. Both the tap and river water samples were acidified by the dropwise addition of 1 M HCl solution accompanied with fast stirring, until a pH of 4 was achieved.

3. Results and discussion

3.1. Morphology and structural properties

Fig. 1a and **b** shows highly oriented, dense and one-dimensional TiO_2 nanorods deposited on the FTO glass substrate. The rods have average diameters of 100–200 nm. **Fig. 1d** and **e** shows scanning electron micrographs (SEM) of $\text{Au-TiO}_2\text{-}2$ nanorods. In comparison with pristine TiO_2 , there was no significant change in the morphology due to the small particle size of Au. The cross-sectional images of pristine and decorated TiO_2 nanorods (**Fig. 1c** and **f**) show that the TiO_2 nanorods grew normal to the FTO glass substrate, leading to a nanorod film thickness of about $2.8 \mu\text{m}$.

To gather more detailed structural information, TiO_2 and $\text{Au-TiO}_2\text{-}2$ were further studied by HRTEM. Lattice fringes are clearly observed as shown in **Fig. 2a**, indicating the crystallinity of the nanorods. The d-spacings for the lattice planes measured were 3.2 and 2.9\AA which are, respectively, in good agreement with the (110) and (001) planes of the rutile TiO_2 phase [25]. The spots (as opposed to rings) in the selected area electron diffraction (SAED) pattern (inset of **Fig. 2a**) surveyed along the [110] zone axis clearly verifies the single crystalline nature of the TiO_2 nanorods. At the same time, HRTEM image in **Fig. 2b** confirmed that the roughly spheri-

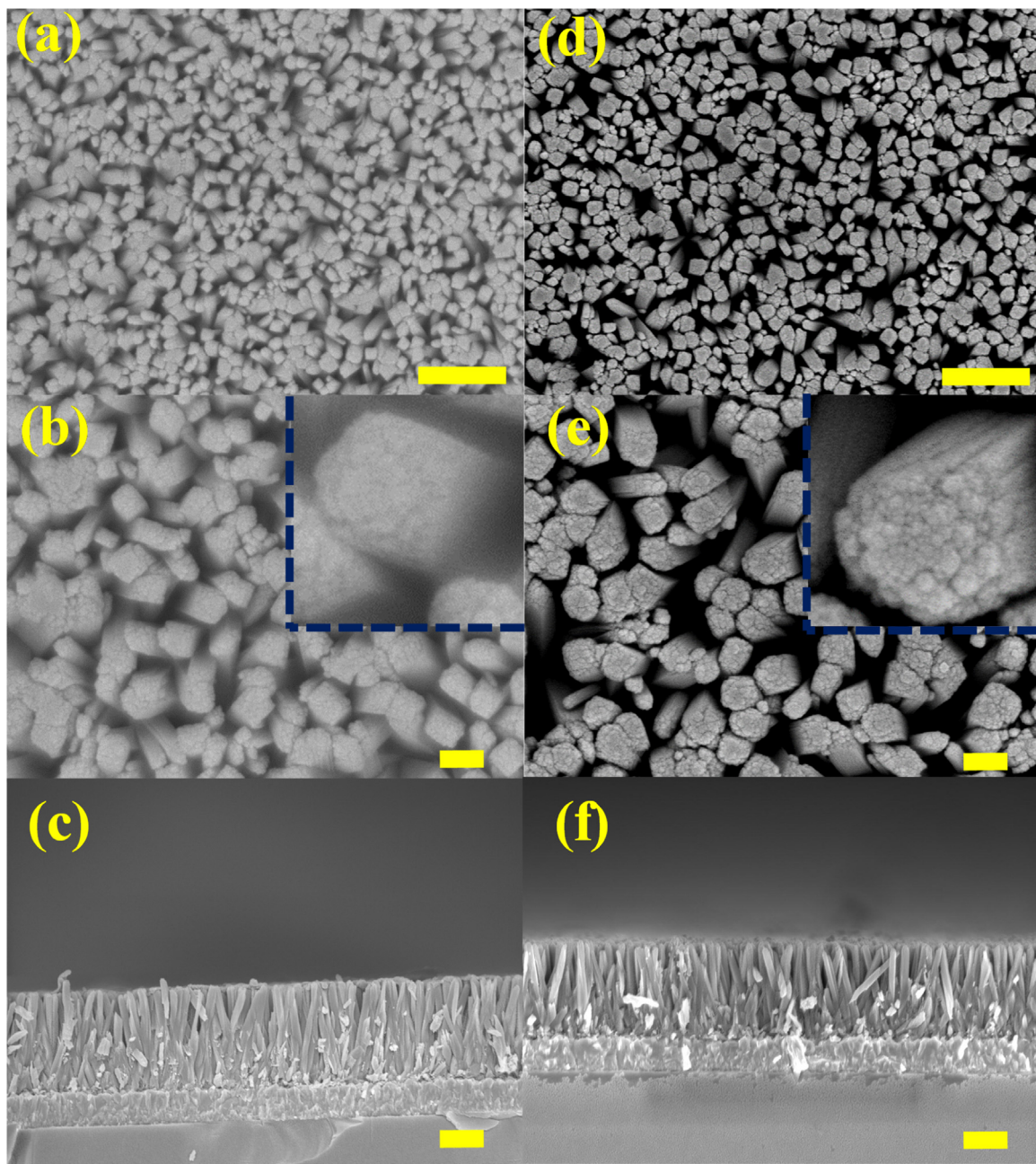


Fig. 1. Top view SEM micrograph of pristine TiO_2 nanorod (a) lower magnification, (b) higher magnification (inset: single nanorod), (c) cross sectional view; Au- TiO_2 -2 (d) lower magnification, (e) higher magnification (inset: single nanorod), (f) cross sectional view; scale bar for (a), (c), (d), (f): 1 μm , and for (b), (e): 200 nm.

cal ~ 10 nm diameter Au nanoparticles (which appeared as darker particles) were homogeneously deposited on TiO_2 nanorods. Inset of Fig. 2b shows well resolved (111) lattice fringes ($d = 0.20$ nm) of Au nanoparticles.

Next, X-ray diffraction (XRD) was utilized to identify the crystal phase of pristine and decorated TiO_2 nanorods. As shown in Fig. 3, all samples were of the TiO_2 rutile phase (JCPDS No: 21-1276) with no additional diffraction peaks that could be attributed to anatase. A small peak was observed at 44.6° that was indexed to the Au (111) plane (JCPDS 04-0784). With increasing deposition cycles, the intensity of this peak increased, indicating successful electrodeposition of Au nanoparticles on the TiO_2 nanorods.

X-ray photoelectron spectroscopy (XPS) was employed to study the chemical states and electrical interaction between the Au nanoparticles and TiO_2 nanorods. Fig. 4a shows two peaks at 458.4

and 464.1 eV, which correlate with the spin-orbit components of Ti^{+4} ($\text{Ti}2\text{p}_{3/2}$ and $\text{Ti}2\text{p}_{1/2}$ respectively) and represent the oxide phase of titanium [26]. A positive shift in $\text{Ti}2\text{p}_{3/2}$ was observed upon deposition of Au, indicating electron transfer between the Au nanoparticles and TiO_2 nanorods [27]. From Fig. 4b, a sharp peak at 530.1 eV and a broad one at 532.2 eV were observed in the O_{1s} spectra, and are attributed to O^{2-} in the TiO_2 lattice and Ti-OH , respectively [28]. The chemical state of Ti and O in the TiO_2 matrix were not affected after Au loading.

Fig. 4c shows two peaks at 83.5 and 87.2 eV corresponding to $\text{Au}4\text{f}_{7/2}$ and $\text{Au}4\text{f}_{5/2}$, indicating the metallic state of the as-deposited Au nanoparticles, which is in agreement with the XRD analysis [29]. It is noteworthy at this point, that a significant negative shift for $\text{Au}4\text{f}_{7/2}$ was observed in comparison with bulk Au (84 eV). This indicates electron transfer from the TiO_2 nanorods to

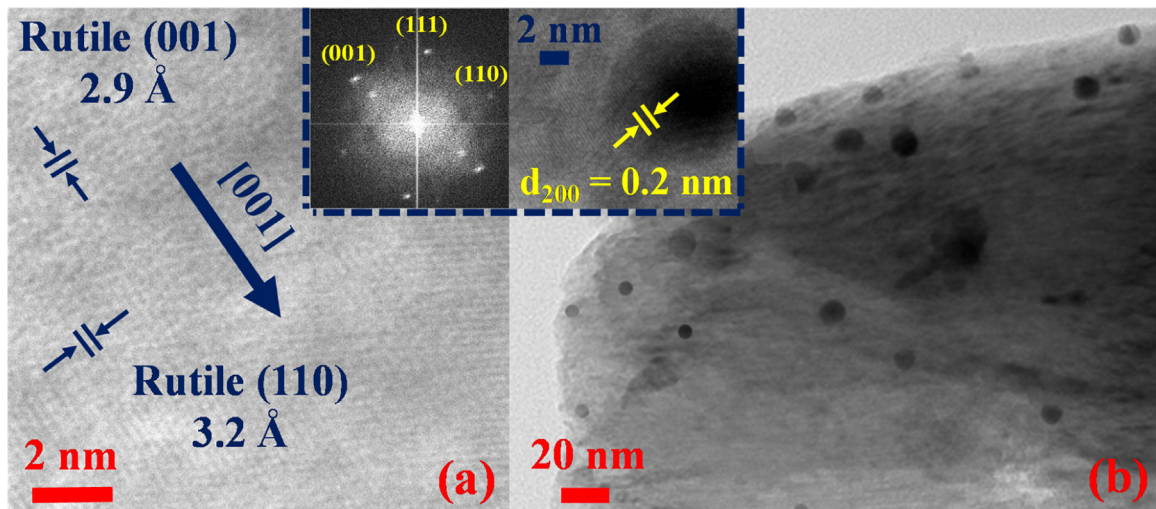


Fig. 2. (a) HRTEM image of pristine TiO_2 (inset: SAED pattern) (b) TEM image $\text{Au}-\text{TiO}_2$ -2 (inset: HRTEM image of single Au nanoparticle).

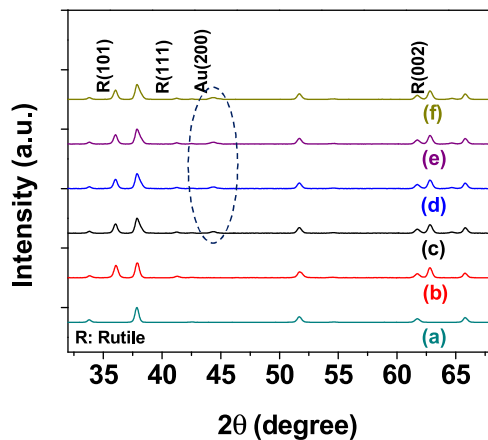


Fig. 3. XRD analysis of (a) FTO glass substrate, (b) TiO_2 , (c) $\text{Au}-\text{TiO}_2$ -1, (d) $\text{Au}-\text{TiO}_2$ -2, (e) $\text{Au}-\text{TiO}_2$ -4, (f) $\text{Au}-\text{TiO}_2$ -8.

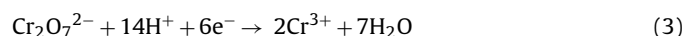
the Au nanoparticles [30]. This transfer occurs due to the difference in the Fermi levels of Au and TiO_2 which results in upward band bending in TiO_2 at the interface with Au (Scheme 1) [31].

Results from UV-vis absorbance measurements in Fig. 5 clearly show that Au decoration of the TiO_2 nanorod photoelectrodes leads to visible-light absorption in the wavelength range from 500 to 600 nm because of the localized surface plasmon resonance (LSPR) effect of the Au nanoparticles. The inset shows that the increase in the LSPR band intensities are linearly related with the number of deposition cycles. It is noticed that the characteristic LSPR absorption band at 540 nm for all decorated photoelectrodes is red shifted in comparison with the plasmon band for Au nanoparticles

in solution (511 nm). This red shift has been attributed to the high refractive index of TiO_2 [32]. In addition, the fact that the LSPR peak wavelength for all samples occurred at approximately the same wavelength indicates that the Au nanoparticles are of similar sizes [33].

3.2. Amperometric detection of Cr(VI)

As shown in Fig. 6a for all samples, there was an increase in the photocurrent after introducing Cr(VI) into the electrolyte, and this can be attributed to the reduction of Cr(VI) to Cr(III). Upon illumination, photogenerated electrons are excited to the conduction band, leaving behind positively charged holes in the valence band of TiO_2 while hot electrons are generated in the Au nanoparticles due to the LSPR effect which can tunnel into the TiO_2 conduction band. All these photogenerated electrons go towards reducing Cr(VI) to Cr(III) if they do not recombine. This can be represented by Eqs. (2) and (3) as follows: [34]



From Fig. 6a, it can also be seen that the photocurrent increases after 1 and 2 cycles of deposition, with the $\text{Au}-\text{TiO}_2$ -2 photoelectrode exhibiting the highest photocurrent, but then decreases to values lower than the undecorated photoelectrode after 8 deposition cycles. This increase can be explained due to two main reasons: (i) in the visible light region, there is an increase in the adsorption of light and hot electrons are injected into the conduction band of TiO_2 due to the strong LSPR effect, and (ii) in the UV region, recombination of charge carriers is depressed as photogenerated electrons and holes are readily separated by favorable band bending at the

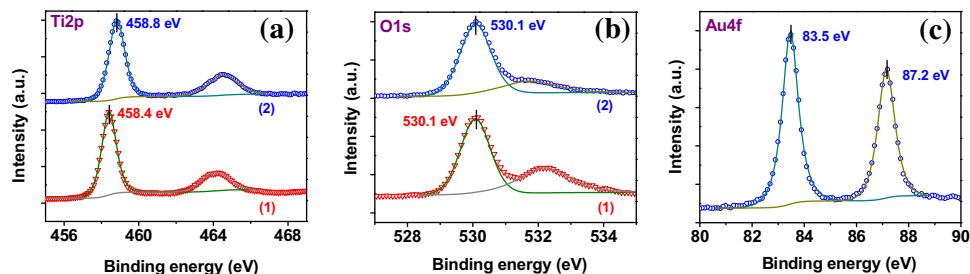
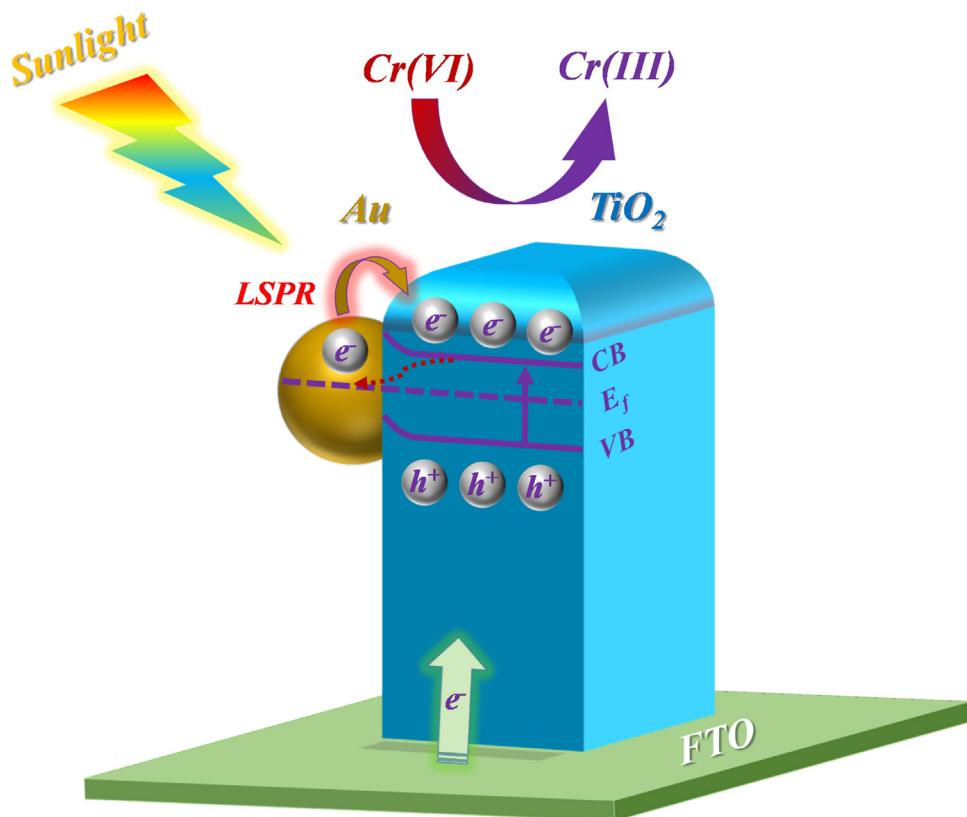


Fig. 4. XPS spectra of (a) $\text{Ti}2\text{p}$ and (b) $\text{O}1\text{s}$ of TiO_2 (1) and $\text{Au}-\text{TiO}_2$ -2 (2); XPS spectra of (c) $\text{Au}4\text{f}$ of $\text{Au}-\text{TiO}_2$ -2.



Scheme 1. Schematic diagram elucidating the PEC reduction of Cr(VI) over Au-TiO₂ under simulated sunlight irradiation.

Au-TiO₂ interface as shown in **Scheme 1** [31]. Further loading of the Au cocatalyst (4 and 8 cycles) decreases the photoelectrocatalytic activity due to screening of surface active sites on the TiO₂ nanorods thus hindering its contact with the electrolyte, and the obstruction of light absorption and thus photogeneration of electrons and holes inside the TiO₂ nanorods. Under visible light only illumination (**Fig. 6b**), the TiO₂ does not generate any photocurrent, whereas the Au-TiO₂-2 photoelectrode showed a photocurrent of 0.26 mA cm⁻². Under UV only radiation, an even larger photocurrent is generated by the Au-TiO₂-2 photoelectrode but at a value still lower than when simulated sunlight is used. This clearly indicates the contribution of the Au cocatalyst.

Using the Au-TiO₂-2 photoelectrode, it was also observed that the pH of the supporting electrolyte played an important role. As shown in **Fig. 6c**, the photocurrent decreases with increasing pH. This is because of the deposition of Cr(OH)₃ on the Au and TiO₂ surfaces at pH > 4.5, thus deactivating the catalysts [35].

Therefore, under the optimal experimental conditions of pH 4 and using the Au-TiO₂-2 photoelectrode, the calibration curves of Cr(VI) in 0.1 mM HCl solution were measured at the potential of -0.2 V vs. SCE (see inset of **Fig. 6d**), resulting in the concentration dependent photocurrent intensity curve of the Au-TiO₂-2 photoelectrode shown in **Fig. 6d**. This plot shows that the increase in photocurrent was proportional to the Cr(VI) concentration in a linear range, from 0.01 to 50 μM, with a detection limit (S/N = 3) and sensitivity of 0.006 μM and 13.94 μA μM⁻¹, respectively. Thus, the suggested protocol can be successfully employed for the monitoring of Cr(VI) in drinking water, as the detection limit is three orders of magnitude lower than the detection requirement of 1 μM, as set by the World Health Organization (WHO) [1].

When compared with other reported values in the literature, **Table 1** shows that the present Au-TiO₂ photoelectrode has the highest sensitivity ever reported among Au-based electrodes for

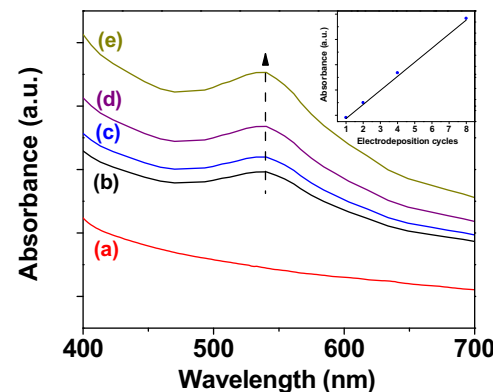


Fig. 5. UV-vis absorption spectra of (a) TiO₂, (b) Au-TiO₂-1, (c) Au-TiO₂-2, (d) Au-TiO₂-4, (e) Au-TiO₂-8.

Cr(VI) detection, in addition to a wide linear range and a low detection limit. This superior sunlight-driven photoelectrochemical performance is due to a combination of factors including fast charge transport along the long axis of the single crystal TiO₂ nanorods, reduced electron–hole recombination due to favorable band bending, enhanced light absorption resulting from the presence of plasmonic Au nanoparticles and a large amount of accessible surfaces due to a dense but open array of nanorods.

3.3. Selectivity, stability, repeatability and reproducibility of the sensor

Selectivity, stability, repeatability and reproducibility are key elements for designing any new sensor. To understand whether the nanostructured photoelectrode could ignore any interference, and

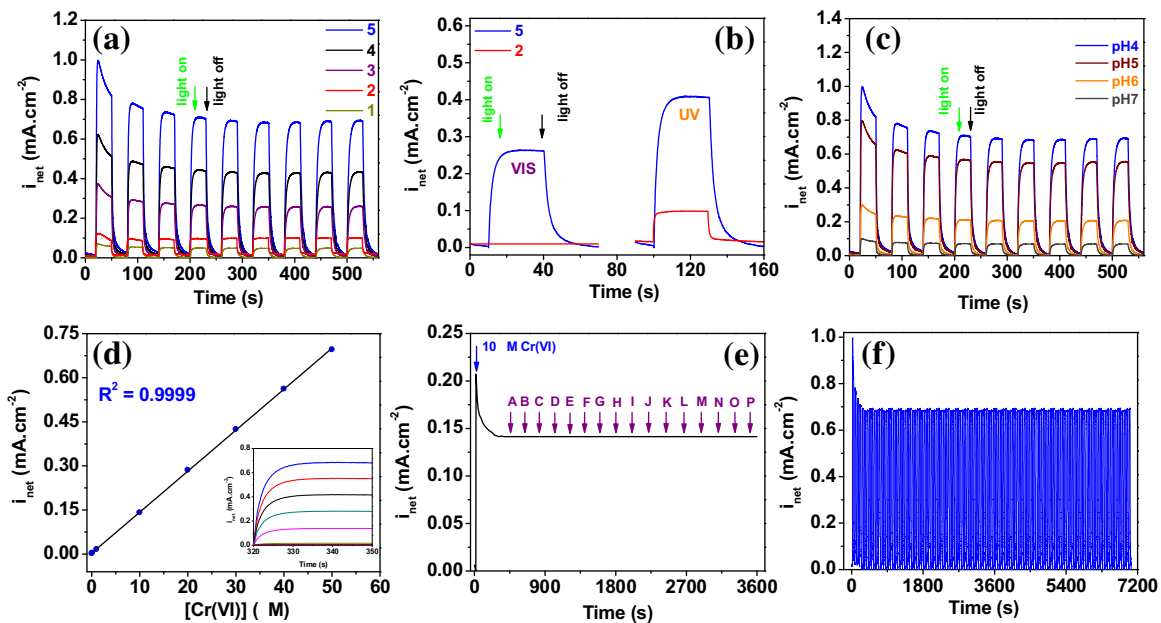


Fig. 6. (a) The photocurrent responses of Au-TiO₂-8 (1), TiO₂ (2), Au-TiO₂-4 (3), Au-TiO₂-1 (4), Au-TiO₂-2 (5), in the presence of 50 μM Cr(VI) at pH 3; (b) The photocurrent responses of TiO₂ (2) and Au-TiO₂-2 (5) under visible and UV light illumination; (c) The photocurrent responses of Au-TiO₂-2 in pH ranges from 3 to 6 (d) Calibration plot of the response photocurrent against the Cr(VI) concentration (inset: The photocurrent responses of the Au-TiO₂-2 photoelectrode as the result of successive addition of Cr(VI) at the potential of -0.2 V in a 0.1 mM HCl solution). (e) The selectivity of the Au-TiO₂-2 photoelectrode at -0.2 V vs. SCE in 0.1 mM HCl solution and presence of 10 μM of Cr(VI), 10,000 μM of (A) Cr³⁺, and 4000 μM of (B) Fe³⁺, (C) K⁺, (D) Mg²⁺, (E) Ca²⁺, (F) Zn²⁺, (G) Pb²⁺, (H) Hg²⁺, (I) Cd²⁺, (J) NO₃⁻, (K) Cl⁻, (L) S₂O₃²⁻, (M) VO₃⁻, (N) MnO₄⁻, (O) MoO₄²⁻ and (P) WO₄²⁻. (f) The photocurrent of the Au-TiO₂-2 photoelectrode at -0.2 V vs. SCE in 0.1 mM HCl solution containing 50 μM Cr(VI) for 100 cycles.

Table 1

Comparison of Cr(VI) detection performance of different Au-based electrodes.

Electrode	Method	Linear Range (μM)	LOD (μM)	Sensitivity (μA μM ⁻¹)	pH	Ref
Au screen-printed macro electrode	LSV*	10–1600	4.4	0.05	1	[4]
Au nanoparticle on ITO	CV**	5–100	2	0.30	2	[8]
Au nanoparticle on ITO	CA***	0.5–50	0.1	0.35	2	[8]
Au nanoparticle on silicate network	CA	0.004–0.057	0.002	1.56	1	[9]
Au nanoparticle on TiO ₂ nanotube arrays	CA	0.1–105	0.03	6.91	1	[36]
Au nanoparticle on TiO ₂ nanorod arrays	PEC-CA	0.01–50	0.006	13.94	4	Present work

* Linear sweep voltammetry.

** Cyclic voltammetry.

*** Chronoamperometry.

still detect and reduce the target analyte, that is Cr(VI), amperometric measurements were performed under sun simulator irradiation at -0.2 V vs. SCE in the presence of foreign ions. Fig. 6e, shows a photocurrent response of about 0.14 mA cm⁻² by injecting 10 μM Cr(VI) into a stirred supportive electrolyte, which is in agreement with the calibration curve in Fig. 6d. No additional responses were observed when injecting a wide range of foreign ions, including 10,000 μM of Cr³⁺, and 4000 μM of Mn⁷⁺, Fe³⁺, Mg²⁺, Ca²⁺, Zn²⁺, Pb²⁺, Hg²⁺, Cd²⁺, CH₃COO⁻, NO₃⁻, Cl⁻, S₂O₃²⁻, VO₃⁻, MoO₄²⁻ and WO₄²⁻. This confirms that the Au-TiO₂ photoelectrode displays good anti-interference ability for the PEC determination of Cr(VI).

In order to examine the stability of the PEC sensor, the photocurrent was recorded consecutively for 100 cycles in the 0.1 mM HCl solution containing 50 μM Cr(VI) (Fig. 6f). A stable photocurrent was observed even after 100 continuous cycles. Even after storage of 3 months, the photocurrent decrease was at most 4%, showing the long-term stability of the photoelectrode.

The repeatability of the Au-TiO₂ photoelectrode was also tested by using the same electrode for 20 repeated amperometric experiment at a potential of -0.2 V vs. SCE under sun simulator irradiation in a solution containing 10 μM Cr(VI). An observed relative standard deviation (RSD) of 1.5% reflects excellent repeatability.

Finally, the reproducibility of the method was examined by fabricating five Au-TiO₂ photoelectrodes from five different

hydrothermal growth runs and performing the amperometric experiment at the potential of -0.2 V vs. SCE under sun simulator irradiation. These five electrodes recorded an RSD value of 2.2% for their photocurrent responses demonstrating their reproducibility.

All these results clearly show that the Au nanoparticle decorated TiO₂ single crystal nanorod based photoelectrode possessed superb selectivity, stability, repeatability and reproducibility for Cr(VI) PEC sensing.

3.4. Photocatalytic tests

As shown in Fig. 7, Cr(VI) can also be reduced photocatalytically. Fig. 7 also clearly shows that the reduction of Cr(VI) is much faster by the PEC process as complete reduction is achieved in 30 min as compared with the 90 min required by the photocatalytic method, indicating the significant synergistic effect of bias potential and sunlight illumination.

3.5. Electrochemical impedance spectroscopy

Electrochemical impedance spectroscopy (EIS) was carried out to extract further information on the carrier dynamics of the photoelectrodes in the dark and under illumination. The well-established R(C(RW)) model was applied to fit the experimental data of the

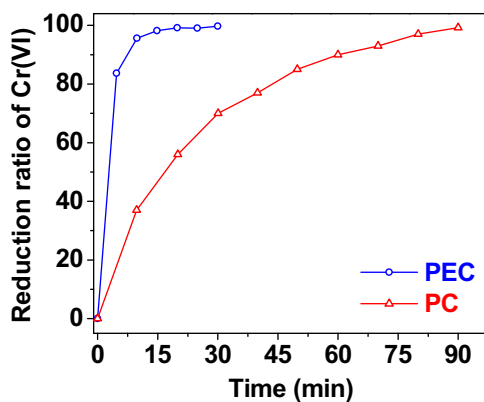


Fig. 7. Reduction ratio of Cr(VI) with reaction time in the photoelectrochemical and photocatalytic processes in 50 mg/L $K_2Cr_2O_7$ aqueous solution under sunlight illumination.

Table 2

Charge transfer resistance obtained from the Nyquist impedance plots.

Sample	R_{ct} under dark ($M\Omega$)	R_{ct} under illumination ($M\Omega$)
TiO_2	1.250	0.835
$Au-TiO_2-2$	0.011	0.006

Nyquist plots (Fig. 8a) under open-circuit conditions and sun simulator irradiation [36].

As shown in Fig. 8b, the measured spectra contained an arc at high frequencies, corresponding to the chemical capacitance of TiO_2 (C_{dl}) and charge transfer resistance (R_{ct}), and a straight line at low frequencies representing the electron diffusion process (W). From Table 2, it can be seen that the charge transfer resistance values were lower under illuminated conditions for both pristine and Au decorated TiO_2 samples, due to the additional photo-induced charges generated by irradiation. More significantly, it is seen that Au decoration leads to a decrease of two orders of magnitude in charge transfer resistance, clearly illustrating the benefits of

favorable band bending and hot electron injection in increasing photocurrent generation.

Consequently, the results of EIS revealed that the $Au-TiO_2-2$ photoelectrode showed higher photoelectrocatalytic activity owing to facilitated electron transfer that is essential for free exchange of the reaction intermediates [37]. The enhanced separation of charge carriers on the decorated TiO_2 nanoparticles offered more efficient channeling of the charge carriers into beneficial reduction reactions rather than unfavorable recombination reactions.

3.6. Measurements in natural media

The proposed PEC sensor was used for the determination of Cr(VI) in tap and river water using the amperometric technique at -0.2 V vs. SCE and under sun simulator illumination in order to evaluate its reliability in real world samples. The samples were spiked with different Cr(VI) concentration after filtering and acidifying with HCl (pH ~ 4). From Table 3, the recovery was found to be from 98.16% to 99.28% and 98.56% to 100.68% for the tap and river water samples, respectively, indicating that $Au-TiO_2$ photoelectrode could be effectively used for the determination of Cr(VI) in real water samples. The results obtained from the PEC sensor was also verified by analyzing the samples using the inductively coupled plasma atomic emission spectroscopy (ICP-AES) technique. The good agreement between our proposed method and ICP-AES indicates that the modified photoelectrode possess good practical application potential for sensing Cr(VI).

4. Conclusion

Single-crystal rutile TiO_2 nanorod arrays were grown hydrothermally on FTO glass substrates at 150 °C. The TiO_2 nanorods were subsequently decorated with Au nanoparticles by cyclic voltammetry and then used as photoelectrodes in a Cr(VI) PEC sensor. It was observed that TiO_2 nanorod photoelectrodes decorated with Au nanoparticles after two cycles displayed the

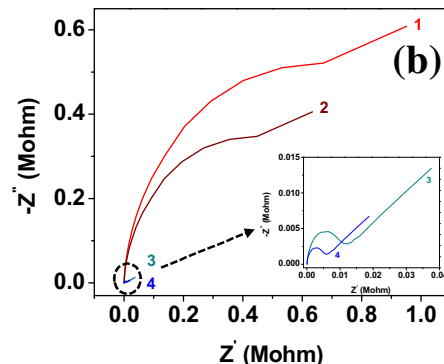
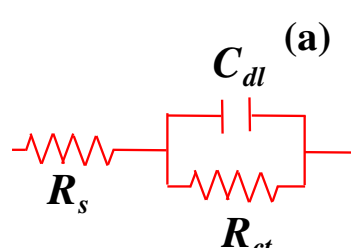


Fig. 8. (a) Equivalent circuit model used for fitting data; (b) Nyquist plots of TiO_2 (1 and 2 in the dark and under illumination, respectively) and $Au-TiO_2-2$ (3 and 4 in the dark and under illumination, respectively) in a 0.1 M KCl solution containing 5 mM $K_3[Fe(CN)_6]$ at open circuit potential and 10 mV amplitude over the frequency range of 10^5 –0.01 Hz. The inset is an enlargement of $Au-TiO_2-2$ spectra.

Table 3

Cr(VI) recovery tests in spiked tap and river water samples ($n=5$).

Sample	Cr(VI) added (μM)	Cr(VI) found (μM)	Recovery (%)	ICP-AES (μM)
Tap	0.5	0.493 ± 0.006	98.62 ± 1.19	0.50
	1	0.982 ± 0.015	98.16 ± 1.51	1.01
	5	4.964 ± 0.062	99.28 ± 1.24	5.02
River	0.5	0.493 ± 0.010	98.56 ± 2.03	0.50
	1	1.007 ± 0.011	100.68 ± 1.06	0.99
	5	4.960 ± 0.058	99.20 ± 1.17	5.09

best properties, with excessive Au loading after eight cycles resulting in photocurrents even lower than for undecorated nanorods. The Au nanoparticle decorated TiO_2 nanorod based PEC sensor demonstrated very high sensitivity of $13.94 \mu\text{A} \mu\text{M}^{-1}$ with a very low detection limit ($S/N=3$) of $0.006 \mu\text{M}$ over a wide linear concentration range from 0.01 to $50 \mu\text{M}$. Electrochemical impedance spectroscopy showed that Au decoration led to a decrease in the charge transfer resistance by more than two orders of magnitude. This decrease is due to two reasons: (i) the LSPR effect at Au nanoparticles leading to an extension of the absorption spectrum into the visible, and (ii) favorable upward band bending in TiO_2 at the interface with Au due to differences in Fermi levels that leads to suppressed charge recombination. Coupled with enhanced charge transport via the long axis of the aligned 1D single crystal TiO_2 nanorods, these factors explain the extremely high sensitivity obtained in this study.

References

- [1] W. Jin, K. Yan, RSC Adv. 5 (2015) 37440–37450.
- [2] U. Thacker, R. Parikh, Y. Shouche, D. Madamwar, Bioresour. Technol. 98 (2007) 1541–1547.
- [3] S. Sultan, S. Hasnain, Bioresour. Technol. 98 (2007) 340–344.
- [4] J.P. Metters, R.O. Kadara, C.E. Banks, Analyst 137 (2012) 896–902.
- [5] Y. Inoue, T. Sakai, H. Kumagai, J. Chromatogr. A 706 (1995) 127–136.
- [6] M.J. Shaw, P.R. Haddad, Environ. Int. 30 (2004) 403–431.
- [7] N. Freslon, G. Bayon, D. Birot, C. Bollinger, J.A. Barrat, Talanta 85 (2011) 582–587.
- [8] M.C. Tsai, P.Y. Chen, Talanta 76 (2008) 533–539.
- [9] B.K. Jena, C.R. Raj, Talanta 76 (2008) 161–165.
- [10] Q. Li, K.J. Morris, P.K. Dasgupta, I.M. Raimundo, H. Temkin, Anal. Chim. Acta 479 (2003) 151–165.
- [11] Y.C. Zhang, M. Yang, G. Zhang, D.D. Dionysiou, Appl. Catal. B Environ. 142–143 (2013) 249–258.
- [12] W. Tu, Y. Dong, J. Lei, H. Ju, Anal. Chem. 82 (2010) 8711–8716.
- [13] A. Kleiman, A. Márquez, M.L. Vera, J.M. Meichtry, M.I. Litter, Appl. Catal. B Environ. 101 (2011) 676–681.
- [14] S. Luo, Y. Xiao, L. Yang, C. Liu, F. Su, Y. Li, et al., Sep. Purif. Technol. 79 (2011) 85–91.
- [15] A. Pandikumar, R. Ramaraj, Mater. Chem. Phys. 141 (2013) 629–635.
- [16] J.J. Testa, M.a. Grela, M.I. Litter, Environ. Sci. Technol. 38 (2004) 1589–1594.
- [17] L. Wu, F. Li, Y. Xu, J.W. Zhang, D. Zhang, G. Li, et al., Appl. Catal. B Environ. 164 (2015) 217–224.
- [18] G. Wen, X. Wen, M.M.F. Choi, S. Shuang, Sens. Actuators B Chem. 221 (2015) 1449–1454.
- [19] G. Wang, H. Jiao, K. Liu, X. Wu, Y. Dong, Z. Li, et al., Electrochim. Commun. 41 (2014) 47–50.
- [20] H. Li, J. Li, Q. Xu, X. Hu, Anal. Chem. 83 (2011) 9681–9686.
- [21] G.-L. Wang, J.-J. Xu, H.-Y. Chen, Nanoscale 2 (2010) 1112–1114.
- [22] Q. Shen, X. Zhao, S. Zhou, W. Hou, J.-J. Zhu, J. Phys. Chem. C 115 (2011) 17958–17964.
- [23] H. Li, J. Li, W. Wang, Z. Yang, Q. Xu, X. Hu, Analyst 138 (2013) 1167.
- [24] B. Liu, E.S. Aydil, J. Am. Chem. Soc. 131 (2009) 3985–3990.
- [25] JCPDS No. 21-1276. (n.d.).
- [26] F. Su, T. Wang, R. Lv, J. Zhang, P. Zhang, J. Lu, et al., Nanoscale 5 (2013) 9001–9009.
- [27] N. Kruse, S. Chenakin, Appl. Catal. A Gen. 391 (2011) 367–376.
- [28] J. Fang, S.W. Cao, Z. Wang, M.M. Shahjamali, S.C.J. Loo, J. Barber, et al., Int. J. Hydrogen Energy 37 (2012) 17853–17861.
- [29] B. Lay, Y.M. Sabri, S.J. Ippolito, S.K. Bhargava, Phys. Chem. Chem. Phys. 16 (2014) 19522–19529.
- [30] Y. Liu, L. Juang, Society 20 (2004) 6951–6955.
- [31] S. Dhara, P.K. Giri, S. Dhara, P.K. Giri, J. Appl. Phys. 110 (2011) 124317.
- [32] L. Du, A. Furube, K. Yamamoto, K. Hara, R. Katoh, M. Tachiya, J. Phys. Chem. C (2009) 6454–6462.
- [33] V. Jovic, W.T. Chen, D. Sun-Waterhouse, M.G. Blackford, H. Idriss, G.I.N. Waterhouse, J. Catal. 305 (2013) 307–317.
- [34] S. Ai, J. Li, Y. Yang, M. Gao, Z. Pan, L. Jin, Anal. Chim. Acta 509 (2004) 237–241.
- [35] X. Wang, S.O. Pehkonen, A.K. Ray, Ind. Eng. Chem. Res. 43 (2004) 1665–1672.
- [36] X. Ding, M. Yang, J. Hu, Q. Li, A. McDougall, Microchim. Acta 158 (2007) 65–71.
- [37] W. Jin, G. Wu, A. Chen, Analyst 139 (2014) 235–241.